JM PAPERS

Coexistence of dual wing–wake interaction mechanisms during the rapid rotation of flapping wings

Long Chen[1,2] and Jianghao Wu[1,†]

[1]School of Transportation Science and Engineering, Beihang University, Beijing 100191, PR China
[2]School of Aeronautic Science and Engineering, Beihang University, Beijing 100191, PR China

Insects flip their wings around each stroke reversal and may enhance lift in the early stage of a half-stroke. The possible lift-enhancing mechanism of this rapid wing rotation and its strong connection with wake vortices are still underexplored, especially when unsteady leading-edge vortex (LEV) behaviours occur. Here, we numerically studied the lift generation and underlying vorticity dynamics during the rapid rotation of a low aspect ratio flapping wing at a Reynolds number (Re) of 1500. Our findings prove that when the outboard LEV breaks down, an advanced rotation can still enhance the lift in the early stage of a half-stroke, which originates from an interaction with the breakdown vortex in the outboard region. This interaction, named the breakdown-vortex jet mechanism, results in a jet and thus a higher pressure on the upwind surface, including a stronger wingtip suction force on the leeward surface. Although the stable LEV within the mid-span retains its growth and location during an advanced rotation, it can be detrimental to lift enhancement as it moves underneath the wing. Therefore, for a flapping wing at $Re \sim 10^3$, the interactions with stable and breakdown leading-edge vortices lead to the single-vortex suction and breakdown-vortex jet mechanisms, respectively. In other words, the contribution of wing–wake interaction depends on the spanwise location. The current work also implies the importance of wing kinematics to this wing–wake interaction in flapping wings, and provides an alternative perspective for understanding this complex flow phenomenon at $Re \sim 10^3$.

Key words: swimming/flying, vortex dynamics

1. Introduction

The marvellous flight skills of insects are underpinned by their high-lift generation of wings, which undergo reciprocating sweeps with rapid wing rotations at stroke reversals to prepare the angle of attack for the next half-stroke (Ellington 1984; Chin & Lentink 2016).

† Email address for correspondence: buaawjh@buaa.edu.cn

Several unsteady aerodynamic mechanisms, such as clap and fling (Weis-Fogh 1973; Cheng & Sun 2019), absence of stall (Ellington *et al.* 1996), and rotational lift (Dickinson 1994; Sun & Tang 2002), have been proposed to explain the failure of steady aerodynamic principles in understanding the high lift generation of insect wings. Among these mechanisms, the absence of stall and its associated physical phenomenon, i.e. the prolonged attachment of a leading-edge vortex (LEV), answer the sustained high lift during most of a half-stroke and thus have been studied extensively (Birch & Dickinson 2001; Sun & Wu 2004; Shyy & Liu 2007; Lentink & Dickinson 2009; Lim *et al.* 2009; Cheng *et al.* 2013; Garmann, Visbal & Orkwis 2013; Jardin & David 2014; Jardin 2017; Chen, Wu & Cheng 2019, 2020; Werner *et al.* 2019; Chen *et al.* 2022*a*, 2023*b*). The rapid wing rotation at stroke reversals and its contribution to lift are more complicated due to the strong unsteadiness and an inevitable interaction with wake vortices. Some studies separate the impacts of wing rotation into two major mechanisms, i.e. rotational lift (or rotational circulation) and wing–wake interaction (or wake capture) (Dickinson 1994; Dickinson, Lehmann & Sane 1999; Birch & Dickinson 2003). The concept of rotational lift originates from the unsteady aerofoil theory and has been modelled in a quasi-steady fashion (Dickinson 1994). In contrast, the wing–wake interaction is rather unpredictable due to its strong dependency on wing kinematics and flow conditions (Wu & Sun 2005).

The wing–wake interaction of a hovering flapping wing involves the vortex system formed in previous strokes. From a more general perspective, the wing–wake interaction also occurs in the clap and fling motion (Cheng & Sun 2019), and between tandem flapping wings (Sun & Lan 2004; Lehmann 2008; Lua *et al.* 2016*b*; Chen, Li & Chen 2022*b*). In this research, the wing–wake interaction is specified around the stroke reversal of a single flapping wing in hovering flight. During this period, the wing flips rapidly to prepare the angle of attack, and interacts with wake vortices simultaneously. This differs from the interaction between the wing and the vortex-induced downwash, which happens in the middle of a half-stroke. Dickinson (1994) and Dickinson *et al.* (1999) named this interaction wake capture, which explained the additional lift benefit in the early stage of a half-stroke. In their dynamically scaled robotic experiments of fruitfly wings, the LEV and trailing-edge vortex (TEV) generated in a half-stroke can pair up as a dipole that induces an inter-vortex jet pointing towards the wing. When the wing encountered this jet in the next half-stroke, the effective incoming velocity was greater than the translating speed of the wing, thus increasing transient lift. However, this was questioned by a parallel three-dimensional (3-D) simulation done by Sun & Tang (2002). They obtained the refined flow data of a fruitfly wing with kinematics similar to Dickinson *et al.* (1999), and the impingement of an inter-vortex jet was absent. Instead, they underscored the prominence of a downwash wake in reducing the effective angle of attack and lift generation in the middle of a half-stroke. Moreover, they proposed the rapid acceleration mechanism as an alternative to explain the lift peak after each stroke reversal. The existence of downwash wake and its adverse effect on lift generation were then evidenced by Birch & Dickinson (2003), in which a decrease in effective angle of attack occurred after the impingement of an inter-vortex jet. In further research on wing kinematic impacts, Wu & Sun (2005) found that the wing–wake interaction can either increase or decrease the transient lift at the beginning of a half-stroke, and this strong kinetic dependency is linked to the evolution of the vorticity field. Kweon & Choi (2010) further demonstrated that the specific mechanism of wing–wake interaction may be related to the spanwise position of the wing because they evidenced a change in the direction of induced wake flows along the span.

In addition to the inter-vortex jet and downwash, there can be another flow phenomenon led by the wing–wake interaction, i.e. the single-vortex suction, which was evidenced by

Kim & Choi (2007) in a deviated flapping aerofoil. This phenomenon is attributed to the approaching of a shed LEV towards the wing and thereby leads to a suction force on the upwind surface due to the low pressure in the vortex core. Lua, Lim & Yeo (2011) conducted two-dimensional (2-D) experiments of flapping wings under two motion styles, i.e. 'acceleration–constant speed–deceleration–stop' and cyclic 'acceleration–constant speed–deceleration'. According to force measurements and flow patterns, they observed both the inter-vortex jet and single-vortex suction mechanisms, and their occurrence is dependent on the flapping velocity profile. Specifically, they simulated a fruitfly wing under advanced rotations, and quantified the connection between the wake vorticity strength (thus the jet impingement) and flapping velocity profile (Lua *et al.* 2017). A reduced deceleration duration can enhance the lift benefits of the wing–wake interaction. A steeper acceleration can also elevate the lift peak at the beginning of a half-stroke, whereas the overall benefit is limited due to a suppressed interacting period. In their other works, the contribution of inter-vortex jet and single-vortex suction mechanisms on lift generation was relevant to the rotation phase (Lua *et al.* 2015), elevating motion (Lua *et al.* 2016*a*), flapping frequency (Dash *et al.* 2018) and pivot location (Sinha, Lua & Dash 2021). One of their recent works focused on the impact of three-dimensionality in geometry and motion (featured by aspect ratio *AR* and Rossby number *Ro*) on this wing–wake interaction (Lee & Lua 2018). Two additional mechanisms – i.e. LEV shedding due to vortex pairing, and the formation of a closely attached LEV – were proposed to amend previous explanations. The former mechanism referred to a perturbation of residual vortex in the wake, and dominated the early LEV shedding on 2-D flapping wings (but diminished in 3-D cases). The latter mechanism represented the rapid formation of a closely attached LEV due to the interaction in 3-D cases, which contributed to lift generation.

Despite the four mechanisms summarized by Lee & Lua (2018), the wing–wake interaction of flapping wings is still underexplored. First, most 3-D research was based on a fruitfly wing at $Re \sim 10^2$. Research on vortex dynamics of 3-D flapping wings has shown that the LEV is stable along the entire span at this Re level (Chen *et al.* 2022*a*). Thus the jet impingement in 3-D cases at $Re \sim 10^2$ may not be fully equivalent to the inter-vortex jet mechanism proposed by Dickinson (1994) because the LEV remains attached and no detached dipole exists in the wake. Second, previous research based on 2-D flapping aerofoils at $Re > 10^3$ is not sufficient to represent 3-D counterparts because the LEV of a 3-D case retains its attachment within the mid-span throughout a stroke, but experiences breakdown near the tip (Chen *et al.* 2022*a*). In contrast, the LEV of a 2-D aerofoil always sheds in a translating motion. This discrepancy in the spatial-temporal status of the LEV can affect the wing–wake interaction because the LEV attachment status has been proven to determine the specific contribution of inter-vortex jet and single-vortex suction mechanisms (Li & Nabawy 2022). Specifically, how the unsteady evolution of an outboard LEV affects the wing–wake interaction is still unclear.

Therefore, following the research of Lee & Lua (2018) and Li & Nabawy (2022), a 3-D flapping wing at $Re = 1500$ with both trapezoidal sweep and rotation was simulated in this work to presumably retain the lift benefit at the beginning of a half-stroke and also to ensure unsteady LEV behaviours near the wingtip. The interaction between the unsteady wake vortices in the outboard region and the newly formed vortices in the following half-stroke is discussed. In § 2, the problem set-up and numerical methods are introduced. An overview of aerodynamic lift generation is given in § 3.1, followed by discussions on flow patterns and vorticity dynamics in § 3.2. The coexistence of dual mechanisms is elaborated in § 3.3, and the transient lift peak after an advanced rotation is explained in
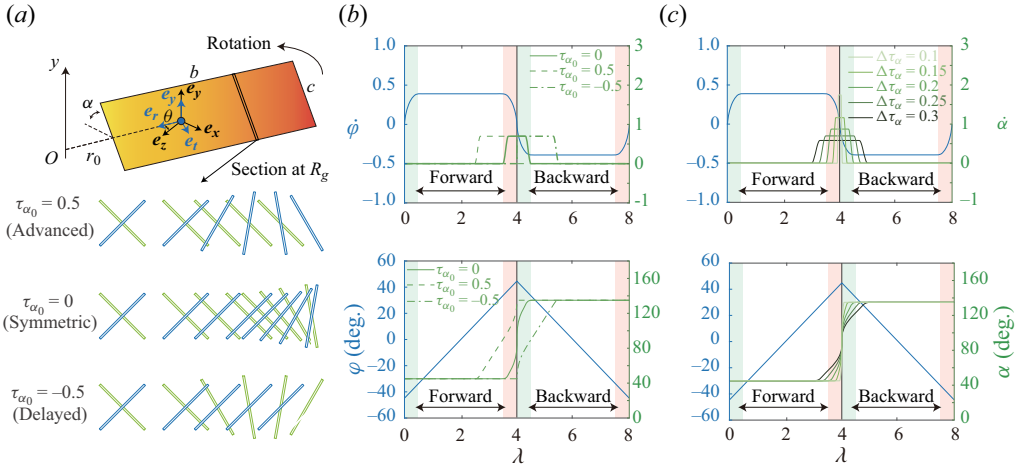
Figure 1. Wing geometry and kinematics: (*a*) the rectangular wing, rotating Cartesian frames, and rotation patterns; (*b*) phase variations (τ_{α_0}); and (*c*) duration variations ($\Delta\tau_\alpha$). Green and red boxes in (*b,c*) denote the acceleration and deceleration periods.

detail in § 3.4. Our findings are then compared to previous works related to this topic in § 3.5. Finally, the remarkable points are concluded in § 4.

2. Methodology

2.1. *Problem set-up*

To mostly retain the low *AR* and *Ro* features of a real insect wing, a rectangular thin plate with $AR = b/c = 3$ (where *b* and *c* are the span and chord; figure 1*a*) is employed. The rectangular plate has been used widely in previous research (Cheng *et al.* 2013; Lee & Lua 2018; Werner *et al.* 2019; Chen *et al.* 2023*a*) as a reasonable geometric simplification of insect wings. The complex motion of insect wings is simplified as a reciprocating sweeping and a rotation along a fixed axis along the span. The sweeping axis is $0.9c$ away from the wing root to account for root cutoff (r_0) effects. In this dimensionless research, the length and velocity references are chord *c* and constant sweeping speed at the radius of gyration (R_g), where

$$R_g = \sqrt{\int_{r_0}^{b+r_0} r^2 \, \mathrm{d}r / b}. \tag{2.1}$$

The sweeping motion follows a form of 'accelerating–constant speed–decelerating' in both forward and backward strokes (figure 1*b*). Specifically, this sweeping is described by an azimuth angle φ, subject to a trapezoidal velocity profile with sinusoidal ramps in each half-stroke. The constant angular speed in sweeping is defined as $\dot{\varphi}_0$, and *Re* based on this constant speed is 1500. To better describe the vortex evolution, a dimensionless time λ, similar to the formation number in relevant research (Poelma, Dickson & Dickinson 2006; Chen *et al.* 2022*a*), is defined as

$$\lambda = \varphi R_g / c. \tag{2.2}$$

The ramps for acceleration and deceleration in sweeping last for only 0.5λ in each half-stroke. The full sweeping amplitude is approximately $90°$, corresponding to a $4c$ travel

987 A16-4

Parameter	Value
Aspect ratio, AR	3
Root cutoff, r_0	0.92
Reynolds number, Re	1500
Flapping amplitude, φ (deg.)	90
Revolving distance at R_g, λ	0–4
Pitching amplitude, $\Delta\alpha$ (deg.)	90
Pitching duration, $\Delta\tau_\alpha$	0.1–0.3
Pitching phase, τ_{α_0}	-0.5 to 0.5

Table 1. Geometric and kinematic parameter set-up.

distance at R_g, which is sufficient to generate a fully developed LEV in this Re regime (Lee & Lua 2018; Chen *et al.* 2022*a*, 2023*a*).

The axis of wing rotation is located at the mid-chord, and the pitching angle (α) denotes the angle between the chord and the horizontal plane (figure 1*a*). Note that α can be over $90°$ in the backward stroke due to the reversed sweeping motion. The wing sustains α at $45°$ and $135°$ during most of the forward and backward strokes, respectively, and a trapezoidal rotation with sinusoidal ramps is imposed around each stroke reversal (figures 1*b*,*c*). The rotation pattern is characterized by its phase relative to the sweeping motion (τ_{α_0}). Here, a positive/negative τ_{α_0} denotes an advanced/delayed rotation, and its magnitude refers to the shift of wing rotation with respect to the stroke reversal. Five typical rotation patterns are investigated in this research, corresponding to $\tau_{\alpha_0} = -0.5$ to $\tau_{\alpha_0} = 0.5$. Here, $\tau_{\alpha_0} = 0.5$, 0 and -0.5 denote fully advanced, symmetric, and fully delayed rotations, respectively. The duration of wing rotation is featured by $\Delta\tau_\alpha$, which evaluates the ratio of rotation duration over the full sweeping period. According to the kinematic data reported by Ellington (1984), $\Delta\tau_\alpha$ is set within 0.1–0.3 to cover the rotation duration of most insect wings. Accordingly, a steeper wing rotation (a lower $\Delta\tau_\alpha$) can enlarge the constant wing rotation speed to achieve an identical wing flip from $\alpha = 45°$ to $\alpha = 135°$. In summary, 25 combinations of τ_{α_0} and $\Delta\tau_\alpha$ are tested in this research, and key geometric and kinematic parameters are listed in table 1.

2.2. *Simulation and data analysis*

Following our previous research on low Re revolving wings (Chen *et al.* 2020, 2022*a*), an in-house solver is used to solve the governing equations, i.e. the 3-D incompressible unsteady Navier–Stokes equations (in the dimensionless form)

$$
\left.
\begin{aligned}
\nabla \cdot \boldsymbol{u} &= 0, \\
\partial \boldsymbol{u}/\partial \tau + (\boldsymbol{u} \cdot \nabla)\boldsymbol{u} + \nabla p - \nabla^2 \boldsymbol{u}/Re &= \boldsymbol{0},
\end{aligned}
\right\}
\tag{2.3}
$$

where $\boldsymbol{u}$ and p denote the dimensionless velocity and pressure. The primary flow quantities are arranged in a node-collocated fashion, and both spatial and temporal discretizations are achieved using second-order schemes (Chen *et al.* 2020). No turbulence model is included in the solver due to the laminar nature of flows at $Re \approx 1000$. The fluid domain is modelled by a cylindrical O-H mesh with $30c$ in both the radius and spanwise directions, and $81 \times 81 \times 91$ nodes in the wing-normal, chordwise and spanwise directions (figure 2*a*). The height of the first layer from the wing surface is $0.001c$, and a half-stroke is evenly
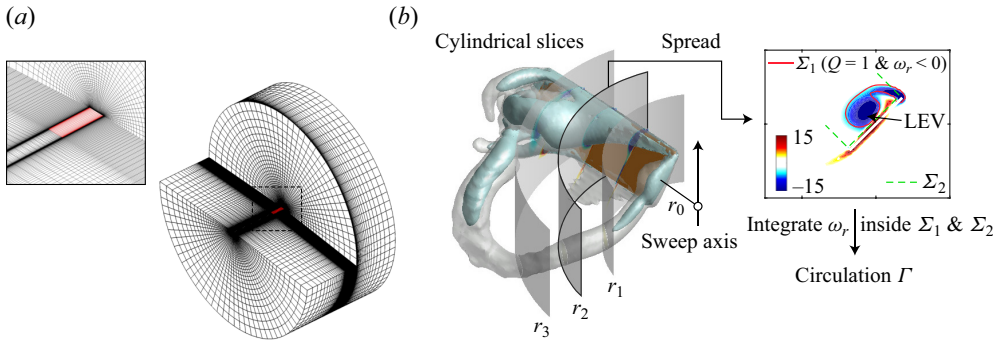
Figure 2. Numerical methods: (*a*) the O-H computational mesh, and (*b*) cylindrical slices, LEV region and integrations. Three slices at radii r_1, r_2 and r_3 are shown here as representatives.

discretized into 400 time steps to resolve all transient variations. The current computational mesh and solver have been thoroughly validated (Chen *et al.* 2018, 2022*a*; Wu *et al.* 2019).

To be consistent with the revolving nature of the wing and its surrounding flow, a set of rotating Cartesian frames is introduced to re-project the data. The rotating Cartesian frame at a specific grid point is relevant to the local azimuth position angle (θ, as shown in figure 1*a*), and can be interpreted as a cylindrical frame. The base axes of this local frame (e_t, e_y, e_r) are defined as follows. The local vertical axis is identical to its global counterpart, and the positive tangential axis points towards the downstream direction. The positive direction of the radial axis is determined by the right-hand rule. This frame system has been employed in our previous flow analysis of pure revolving wings (Chen *et al.* 2019, 2020, 2022*a*), and all vectors in the inertial frame can be transformed into rotating Cartesian frames through a rotating matrix.

According to vorticity and vortex dynamics (Wu, Ma & Zhou 2007), the evolution of vortex structure is dictated by the vorticity transport equation, taking the following dimensionless form in the inertial frame:

$$\partial \boldsymbol{\omega}/\partial \tau = -(\boldsymbol{u} \cdot \boldsymbol{\nabla})\boldsymbol{\omega} + (\boldsymbol{\omega} \cdot \boldsymbol{\nabla})\boldsymbol{u} + \nabla^2 \boldsymbol{\omega}/Re, \tag{2.4}$$

where $\boldsymbol{\omega}$ is vorticity. The terms on the right-hand side of (2.4) are convection, vortex tilting/stretching and diffusion, respectively. In this research, the vorticity dynamics of the LEV (which is mostly occupied by radial vorticity) is our focus, thus (2.4) is projected into the radial direction as follows:

$$\partial \omega_r/\partial \tau = -(\boldsymbol{u} \cdot \boldsymbol{\nabla})\omega_r + (\boldsymbol{\omega} \cdot \boldsymbol{\nabla})u_r + \nabla^2 \omega_r/Re, \tag{2.5}$$

with

$$-(\boldsymbol{u} \cdot \boldsymbol{\nabla})\omega_r = \underbrace{-u_t \, \partial\omega_r/\partial t}_{C_{rt}} \underbrace{- u_y \, \partial\omega_r/\partial y}_{C_{ry}} \underbrace{- u_r \, \partial\omega_r/\partial r}_{C_{rr}}, \tag{2.6}$$

$$(\boldsymbol{\omega} \cdot \boldsymbol{\nabla})u_r = \underbrace{\omega_t \, \partial u_r/\partial t + \omega_y \, \partial u_r/\partial y}_{T_r} + \underbrace{\omega_r \, \partial u_r/\partial r}_{S_r}. \tag{2.7}$$

Here, C_{ri} ($i \in \{t, y, r\}$) denotes the convection of radial vorticity driven by tangential, vertical and radial flows, T_r is the vortex tilting of tangential and vertical vorticity components into the radial direction, and S_r is the vortex stretching (or compression)

in the radial direction. Thus the evaluation of radial vorticity is underpinned by the spatial-temporal variation of vorticity transport terms defined in (2.5)–(2.7).

To quantify the LEV intensity, 40 cylindrical slices (evenly distributed along the wing span) are cut through the flow domain and are then spread into planes (figure 2b). The number of cylindrical slices has been validated to ensure discretization-independent results. The distribution of radial vorticity within each slice is thus illustrated, and the local LEV circulation (Γ) is represented by an integral of radial vorticity (ω_r) within the LEV region. Here, two boundaries Σ_1 and Σ_2 are first identified, and their intersection is used to best outline the LEV region on each cylindrical slice. The first boundary Σ_1 is based on the Q criteria (Q as the second invariant of velocity gradient; Jeong & Hussain 1995) and local radial vorticity. According to a sensitivity study in our previous research (Chen *et al.* 2022a), the LEV circulation becomes saturated when Q reaches 1. Thus the threshold for Σ_1 is $Q = 1$ and $\omega_r < 0$. However, the first boundary Σ_1 can include not only the LEV but also other wake vortices with the same sign. Therefore, the second boundary Σ_2 is introduced as a further constraint to exclude wake vortices. This boundary outlines a rectangular region above the leeward surface, with its front and rear boundaries perpendicular to the leading edge and trailing edge, respectively. To exclude extremely large vorticity values near the wing surface (akin to the issue in Werner *et al.* 2019), a tiny gap of $0.02c$ is introduced between Σ_2 and the leeward surface. The upper limit of Σ_2 is removed since Σ_1 has already identified the upper boundary of the LEV. Moreover, the boundary Σ_2 is identical at all cylindrical slices and is retained throughout the motion.

3. Results

3.1. *Overview of lift generation*

The lift generation of all cases is summarized in figure 3, with the lift coefficient (C_L) as the lift normalized by $0.5\rho(\dot{\varphi}_0 R_g)^2 bc$. The first cycle is analysed here, and the cycle-averaged lift coefficient is the mean of C_L over this cycle. According to a pre-validation, a comparison of the forward and backward strokes within the first cycle can mostly unfold the physics of wing rotation under a fully developed flow condition. As shown in figure 3(a), an advanced rotation ($\tau_{\alpha_0} > 0$) can outperform either a symmetric rotation or a delayed rotation at almost all rotation durations ($\Delta\tau_\alpha$) in this research. However, even a slightly delayed rotation can significantly attenuate the cycle-averaged lift. Within our parameter space, the impact of $\Delta\tau_\alpha$ on the cycle-averaged lift is trivial for symmetric rotations, while a milder rotation (a larger $\Delta\tau_\alpha$) can reduce the lift benefit of advanced rotations and enlarge the lift loss of delayed rotations. Therefore, the lift maximum within our parameter space is achieved by a rapid advanced rotation ($\tau_\alpha = 0.25$ to $\tau_\alpha = 0.5$, and $\Delta\tau_\alpha < 0.2$).

The wing sections of three typical rotation patterns at $\Delta\tau_\alpha = 0.2$ are shown in figure 3(b) (with force vectors), and more detailed transient lift profiles of advanced, symmetric and delayed rotations are compared in figure 3(c). According to figure 3(c), the transient lifts of all rotation patterns have reached an identical steady state in the forward stroke before rotations ($\lambda = 2$–4), corresponding to a fully developed LEV. Also, regardless of rotation patterns, the transient lift recovers to a similar level (a steady C_L close to 2) before the end of the backward stroke ($\lambda = 7.5$), proving that the 4-chord-length travel is sufficient to eliminate the influence of wing rotation on the steady-state lift. For a fully delayed rotation ($\tau_\alpha = -0.5$), the transient lift experiences evident reduction since the onset of wing rotation ($\lambda = 4$) and then recovers gradually ($\lambda = 4$–6 in figure 3c-iii). A milder delayed rotation (a larger $\Delta\tau_\alpha$) can enlarge this lift loss. As shown by the

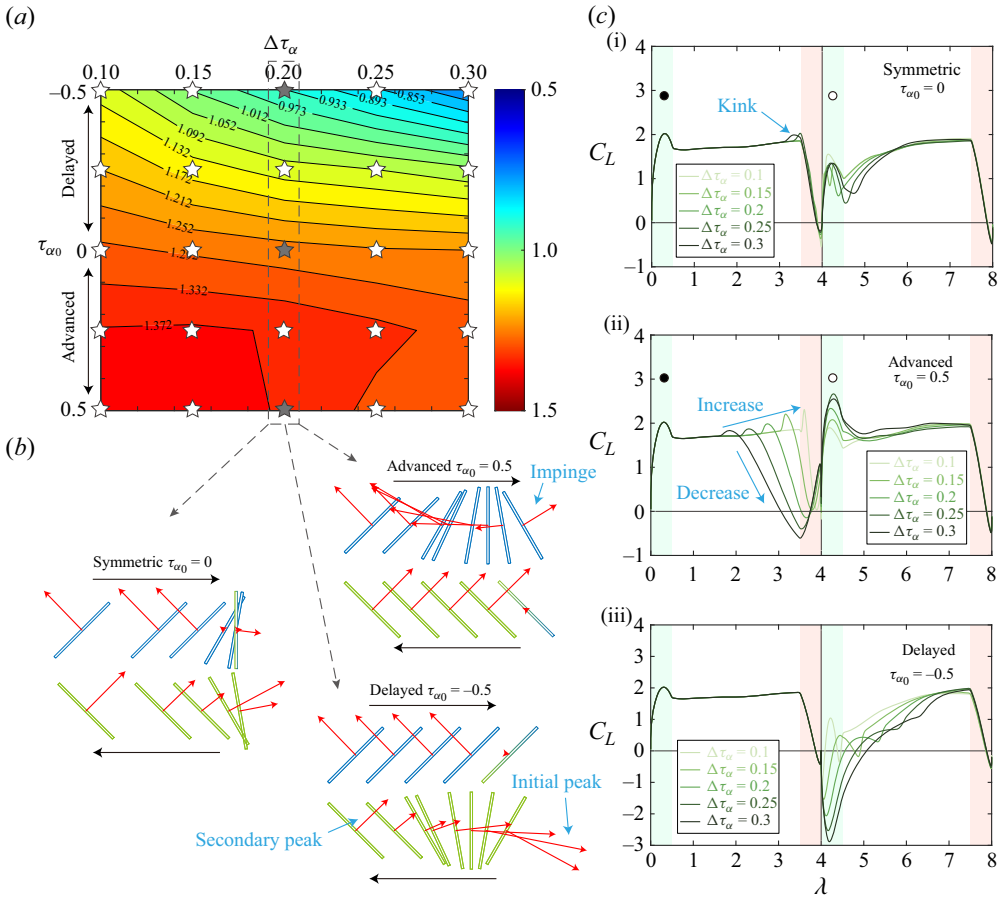Figure 3. Analysis of lift generation: (*a*) cycle-averaged lift; (*b*) diagram of typical wing motions indicating magnitude and orientation of force vectors (red arrows); and (*c*) transient lift.

diagrams in figure 3(*b*), despite the total aerodynamic force being enhanced at the beginning of the backward stroke in the fully delayed pattern, the transient wing posture results in a downward projection, i.e. a negative lift. As the nose-down rotation proceeds, the initial peak of the total aerodynamic force is reduced and then increases to a secondary peak in the constant-speed sweeping.

For symmetric rotations ($\tau_\alpha = 0$), as $\Delta\tau_\alpha$ increases, the lift benefits over the nose-up rotation period are mostly featured by a slight kink before the deceleration of the forward stroke ($\lambda = 3$–4 in figure 3*c*-i). Once the forward stroke enters its deceleration, the transient lift is manipulated by the change in sweep speed other than the variation of $\Delta\tau_\alpha$ (i.e. the reduced rotation rate). In the following backward stroke, a steeper symmetric rotation (a lower $\Delta\tau_\alpha$) can enhance the lift peak in the early stage of the acceleration and then result in a faster recovery towards the steady-state lift. Meanwhile, the contribution of this lift peak in the cycle-averaged lift is limited at a steeper rotation because it lasts for a shorter period (figure 3*c*-i). Thus the effect of $\Delta\tau_\alpha$ on the cycle-averaged lift of a symmetric rotation pattern is marginal. More importantly, regardless of $\Delta\tau_\alpha$, the lift peak in the acceleration of the backward stroke (white circle in figure 3*c*-i) is inferior to its counterpart in the forward stroke (black circle in figure 3*c*-i). Since the pitching angle (α)

is fixed in the acceleration of the forward stroke (black circle in figure 3*c*-i), this implies that the nose-down rotation during the start of each stroke in a symmetric pattern can postpone the LEV formation. Note that in the backward stroke, the wing also interacts with the wake vortices (including an LEV) formed in the forward stroke, and no remarkable lift benefit occurs in the symmetric rotation.

For fully advanced rotations ($\tau_\alpha = 0.5$), the wing has just finished the rotation at the stroke reversal, thus the kinematics of forward and backward strokes are identical, except that the backward stroke involves the wing–wake interaction. As shown in figure 3(*c*-ii), akin to the symmetric pattern, the start of rotation first triggers a slight lift increase, followed by a continuous lift reduction until the stroke deceleration ($\lambda = 2$–4). According to the diagrams in figure 3(*b*), this lift reduction in the advanced pattern is mostly attributed to the anticlockwise rotation of the aerodynamic force vector, thus the enlarged aerodynamic force during this period is mostly transformed into drag. As the wing enters the backward stroke, the lift can jump up to a sufficiently higher value (white circle in figure 3*c*-ii) than that at the same phase in the forward stroke (black circle in figure 3*c*-ii). This phenomenon occurs at $\Delta\tau_\alpha > 0.15$ and becomes prominent at approximately $\Delta\tau_\alpha = 0.25$, indicating that the lift benefits of an advanced rotation are valid only when the wing–wake interaction occupies a sufficient period of the stroke. A higher lift peak in the acceleration of the backward stroke can further promote lift recovery in the rest stroke. However, the lift loss in the forward stroke ($\lambda = 2$–4) dominates the overall lift variation over $\Delta\tau_\alpha$ (figure 3*c*-ii). Therefore, the impact of a milder advanced rotation (a higher $\Delta\tau_\alpha$) and its connection with a beneficial wing–wake interaction is twofold. On the one hand, the disadvantage manifests as an earlier trigger of lift reduction that otherwise should occur later in the deceleration of the forward stroke. This lift reduction is mostly subject to a re-projection of aerodynamic force, and becomes more remarkable as the rotation duration increases. On the other hand, due to the wing–wake interaction, a longer rotation duration can lead to an enhanced lift peak in the acceleration of the backward stroke, contributing to lift enhancement. This benefit has nothing to do with the force projection and is solely related to flow physics, thus supporting the benefit of advanced rotations in flapping wings.

3.2. *Flow analysis*

3.2.1. *Flow structure evolution*

In this subsubsection, the flow pattern and vorticity dynamics of three typical rotation patterns (symmetric, fully advanced and fully delayed, $\Delta\tau_\alpha = 0.2$) are examined to uncover the physics that dominates the impacts of the wing–wake interaction. The transient vortex structures ($Q = 1$ for vortex boundaries in grey, and $Q = 6$ for vortex cores in cyan) during the rotation are displayed in figure 4 and their further evolutions in the backward stroke are shown in figure 5. For a symmetric rotation ($\tau_\alpha = 0$), the LEV in the inboard region tends to lose its conical structure as the wing pitches up in the deceleration of the forward stroke (figure 4), and, simultaneously, the unsteady vortex structures in the outboard region start to break down into sub-structures (breakdown vortex, BDV). Despite this, the entire vortex structure retains its attachment to the leeward surface until the reversal. As the wing enters the backward stroke and passes through the BDV, a tip vortex (TV) is quickly formed, together with the formation of an LEV beyond the mid-span, and they both elongate into the wake as the wing sweeps.

In contrast, when the rotation is fully advanced ($\tau_\alpha = 0.5$), the LEV degradation and the formation of BDV during the pitch-up are weaker since the wing still sweeps forward and the feeding shear layer is less reduced. By the end of the rotation, since no backward
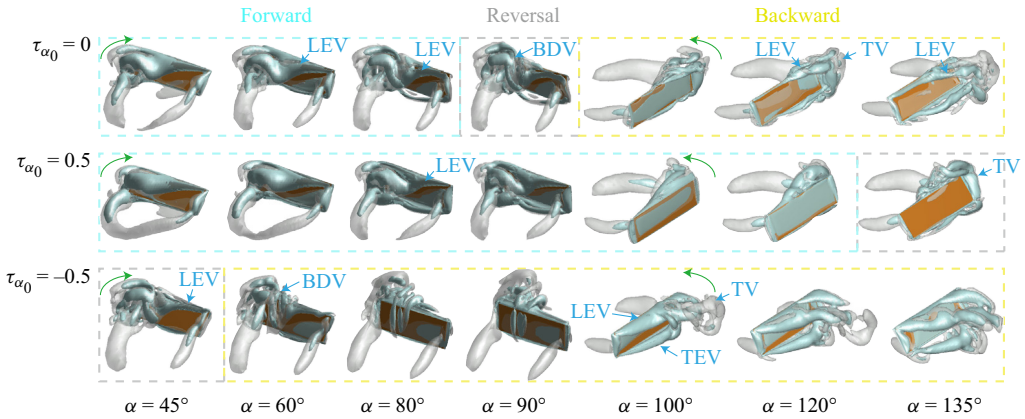
Figure 4. Transient vortex structures of different rotation patterns. The cyan, grey and yellow boxes indicate stroke phases. The camera orientation at $\alpha = 100°$–$135°$ is flipped to show the other wing surface (the lighter isosurfaces). The sweep direction is labelled by a green arrow.
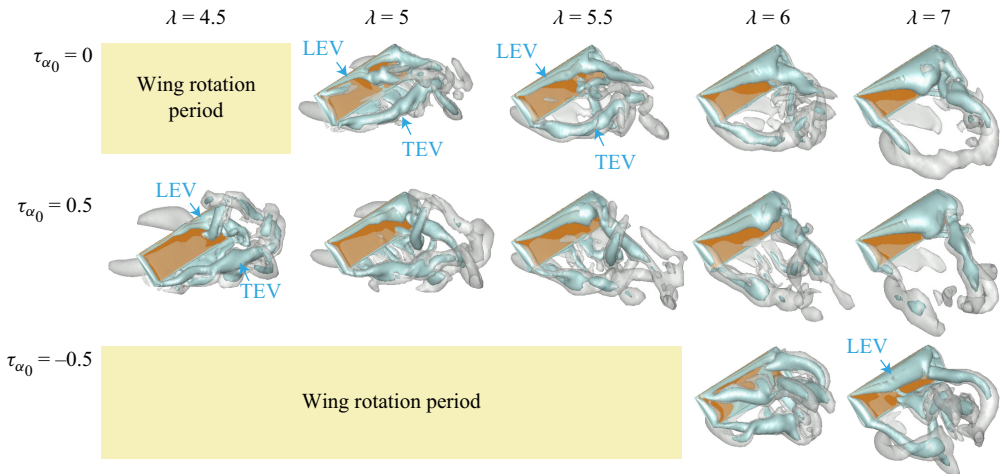

Figure 5. Evolution of vortex structures in the backward stroke after three typical rotations.

stroke is imposed, the impingement of BDV only produces an attached horseshoe-like vortex system in the outboard region, including a TV. Moreover, in the backward sweep (figure 5), this horseshoe-like vortex system can initiate the formation of an attached LEV around the distal corner of the wing, despite the vortices along other edges all shed into the wake. As the sweep speed increases in the backward stroke, this locally attached LEV merges with the conventional LEV within the mid-span as a new conical structure. In addition, compared to the backward stroke after the symmetric rotation, the transient LEV after the fully advanced rotation is stronger at an identical time interval ahead of the steady state ($\lambda = 5$ and 5.5). This is because the shed LEV induced by the BDV of the symmetric rotation fails to connect with the newly formed LEV in the backward stroke and thus postpones the overall LEV growth.

Although the lift performance of a delayed rotation discourages its application in flapping wings, its global vortex structures are also compared in figures 4 and 5. After the reversal, the BDV in the outboard region becomes further chaotic, and the wing encounters
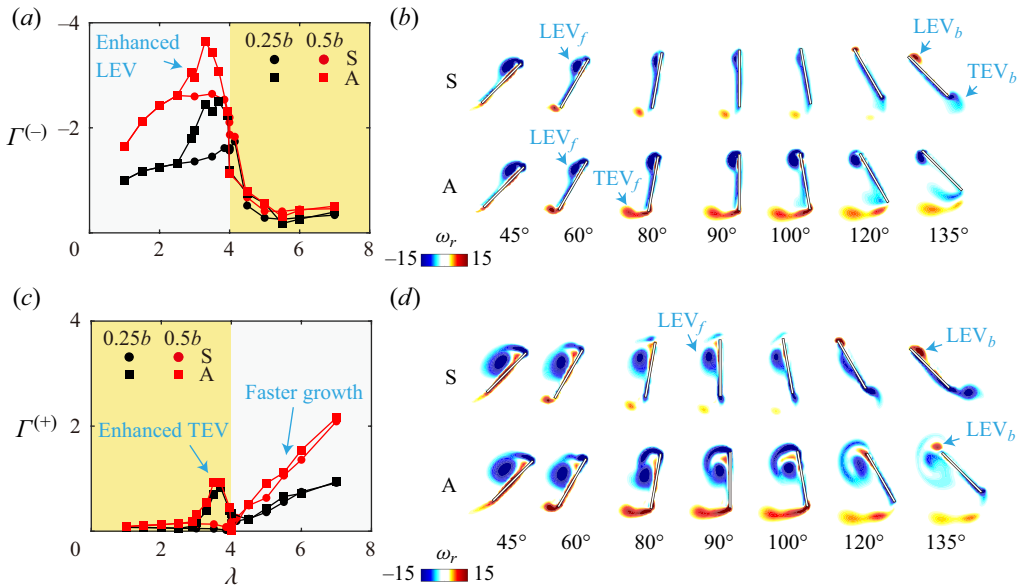
987 A16-10

Figure 6. Intensity of radial vorticity at two representative slices: (*a*) $\Gamma^{(-)}$, (*b*) contours at 0.25*b*, (*c*) $\Gamma^{(+)}$, and (*d*) contours at 0.5*b*. Here, S and A are the symmetric and fully advanced rotations, respectively.

a stronger impingement with the BDV, which is promoted by both the backward stroke and a nose-down rotation. Meanwhile, the transient pitching angle (α) is close to 90° when the wing enters the acceleration of the backward stroke. These two factors both enhance the feeding shear layer at the leading edge and trailing edge, thus leading to significantly stronger LEV and TEV (figure 4, $\alpha = 100°$). Despite the rapid growth, these two vortices quickly shed from edges (figure 4, $\alpha = 120°$ and 135°), and a secondary LEV is formed along the span until the end of the backward stroke (figure 5, $\lambda = 6$–7). Together with the transient lift diagrams reported in figure 3(*b*), the shedding of primary LEV and TEV explains the inferior aerodynamic force in the second half of the fully delayed rotation. Due to the undesirable impacts of delayed rotations, the following sections focus mainly on the comparison between symmetric and fully advanced rotations.

3.2.2. *Vorticity dynamics analysis*
In this subsubsection, a further comparison of the distinct vorticity evolution between symmetric and fully advanced rotations is provided. Sectional analysis at two representative slices (0.25*b* and 0.5*b*) within the stable LEV region is first shown in figure 6. According to the coordinate and integration procedure (§ 2.2), negative and positive circulations $\Gamma^{(-)}$ and $\Gamma^{(+)}$ can mostly represent the LEV intensity in the forward and backward strokes, respectively (as in the grey boxes in figures 6(*a*,*c*). Moreover, the data points in the yellow box denote the TEV intensity in the corresponding stroke.

It is evident that the LEV intensity starts to increase when the wing pitches up ahead of the reversal (figure 6(*a*), $\lambda = 3$–4, advanced rotation); otherwise, the LEV maintains the steady-state value until the deceleration, when an abrupt decrease occurs (figure 6(*a*), $\lambda = 3$–4, symmetric rotation). This LEV enhancement of the advanced rotation is accompanied by a simultaneous increase in TEV intensity (figure 6(*c*), $\lambda = 3$–4, advanced rotation), implying the generation (and then shedding) of an additional TEV to dynamically sustain the Kelvin circulation theorem. In the backward stroke, the LEV is subject to slightly
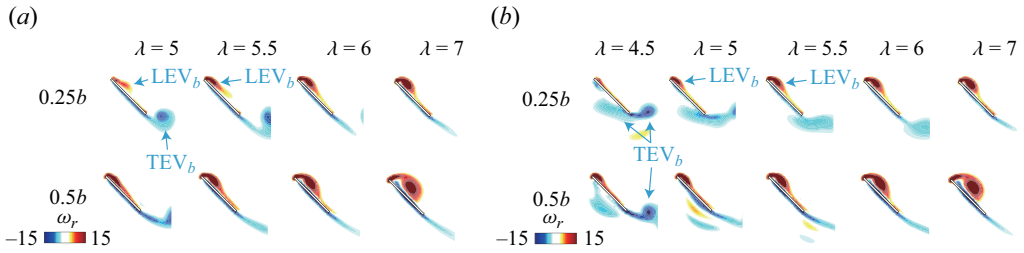
Figure 7. Sectional plots of radial vorticity in the backward stroke: (*a*) symmetric rotation and (*b*) fully advanced rotation.

faster growth when an advanced rotation is imposed. Note that in the backward stroke after both rotations, the LEV cannot reach the steady-state intensity of an impulsive-start stroke ($\lambda = 0$–4), indicating that, in general, the growth of a stable LEV on reciprocating wings is attenuated within most of a stroke due to wake effects. This agrees with Wu & Sun (2005), that the downwash can be detrimental to the LEV growth of insect-like flapping wings.

According to the contours of the radial vorticity component shown in figures 6(*b,d*), when the wing undertakes a symmetric rotation, the vorticity feeding from the shear layer is terminated during the pitch-up, and the LEV_f in the forward stroke is convected towards the trailing edge. The LEV_f tends to be elongated along the lower surface and then merges into the TEV_b in the backward stroke. In contrast, the vorticity feeding from the shear layer is retained over the entire advanced rotation, therefore the LEV_f keeps growing until the stroke reversal, together with the shedding of a stronger additional TEV_f. Almost no convection of LEV_f is seen during an advanced rotation, and the majority of the LEV_f is retained around the leading edge until the wing enters the backward stroke, acting as a vorticity storage for wing–wake interaction.

For the vortex evolution post rotations (figure 7), the stable LEV_b after the advanced rotation achieves a higher intensity than that after the symmetric rotation in the first half of the backward stroke ($\lambda = 5$–6). Note that the contours after the symmetric rotation at $\lambda = 4.5$ have been shown in figures 6(*b,d*) ($\alpha = 135°$). The transient LEV_b after the symmetric rotation is stronger at $\lambda = 4.5$, but it elongates and sheds from the leading edge during $\lambda = 4.5$–5, corresponding to the 3-D plots in figure 5. Moreover, for the advanced rotation, the residual negative vorticity below the lower surface moves towards the trailing edge during $\lambda = 4$–5, and boosts the formation and shedding of the TEV_b. At an identical time instance, the TEV_b after the advanced rotation is convected further downstream (out of the window), indicating a more rapid expansion of the vortex loop (featured by LEV_b, TEV_b, TV and root vortex) and thus a higher transient lift (Sun & Wu 2004). When the backward stroke proceeds into its second half ($\lambda = 6$–8), less difference in the LEV_b intensity and location is observed, leading to comparable LEV_b circulation (figure 6*c*) and lift generation (figure 3*c*).

The critical radial vorticity transport terms are then examined to explain two unique features in the LEV evolution of the advanced rotation (figure 8), i.e. the absence of convection towards the trailing edge during the rotation, and the rapid growth of TEV_b and LEV_b. As the wing pitches up towards 90°, downward convection of the radial vorticity ($C_{ry}^{(+)}$, positive C_{ry} to negative C_{ry}) occurs in the stable LEV region, which is almost perpendicular to the stroke plane and drives the movement of LEV_f towards the trailing edge (figure 8*a*). Here, $C_{ry}^{(+)}$ is located within the entire stable LEV region for the symmetric rotation, while that of the advanced rotation is limited within a smaller
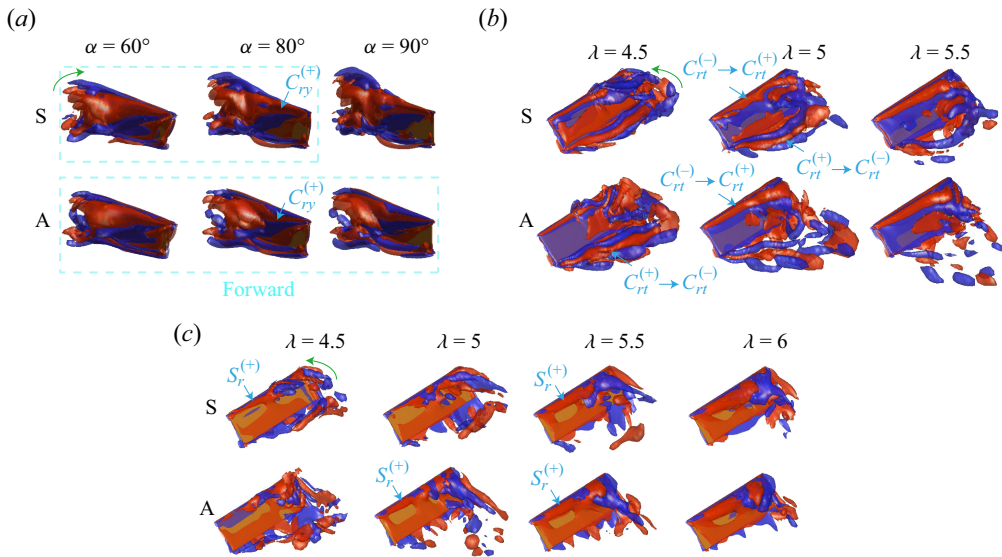
987 A16-12

Figure 8. Critical radial vorticity transport terms within/post typical rotations: (*a*) vertical convection, (*b*) tangential convection, and (*c*) vortex stretching. The isosurfaces are outlined by 6 (red) and −6 (blue).

region in the chordwise direction, and another negative C_{ry} occurs along the leading edge to terminate sustained $C_{ry}^{(+)}$.

Moreover, the merge of the negative radial vorticity into TEV_b during the advanced rotation can be demonstrated by the tangential convection of the radial vorticity component (figure 8*b*), i.e. $C_{rt}^{(+)} \rightarrow C_{rt}^{(-)}$ for the downstream convection of negative vorticity component in TEV_b, and $C_{rt}^{(-)} \rightarrow C_{rt}^{(+)}$ for the downstream convection of positive vorticity component in LEV_b. At $\lambda = 4.5$, the downstream convection of TEV_b is prominent and propagates into the wake during the advanced rotation, which is comparable to that at $\lambda = 5$ for the symmetric rotation. Thus it is suggested that the residual negative vorticity component generated in the forward stroke can promote this downstream convection and thus shift the TEV_b further away from the wing. Meanwhile, the downstream convection of LEV_b during the symmetric rotation experiences a less regular variation over $\lambda = 4$–5 because a conical $C_{rt}^{(-)} \rightarrow C_{rt}^{(+)}$ is first established at $\lambda = 4.5$ and then levels off along the span at $\lambda = 5$. However, the downstream convection of LEV_b during the advanced rotation is consistently enhanced in a conical form along the span since $\lambda = 4$, representing a sustained and regular vorticity feeding from the shear layer, and thus a more rapid growth of LEV_b.

In addition, the vortex stretching ($S_r^{(+)}$) within the LEV_b after the symmetric rotation also has remarkable transient variations during $\lambda = 4$–5 (figure 8*c*), in that an $S_r^{(+)}$ value has been established at $\lambda = 4.5$ and then disappears at $\lambda = 5$. Another conical $S_r^{(+)}$ is formed as the wing sweeps forward to $\lambda = 5.5$. This re-establishment of $S_r^{(+)}$ is not observed in the advanced rotation, and a single conical $S_r^{(+)}$ is maintained and enhanced gradually until $\lambda = 6$.
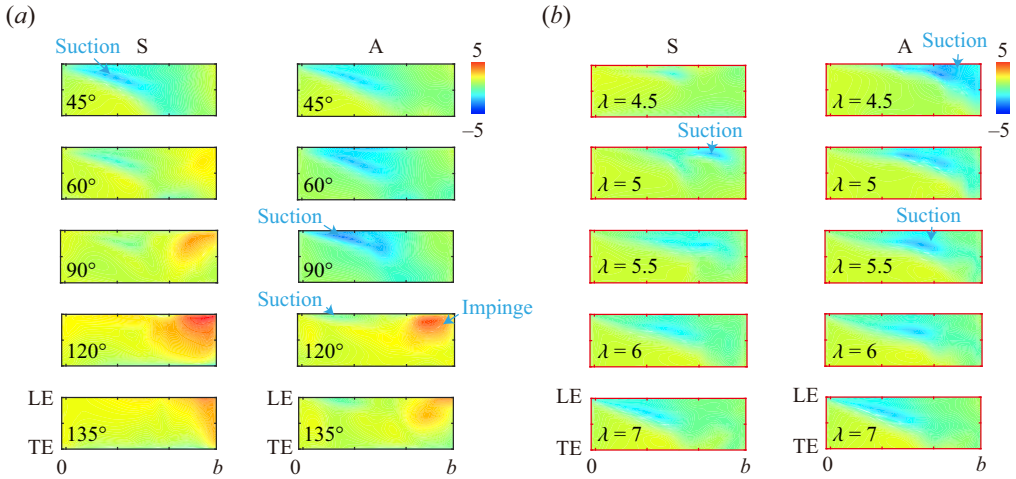
Figure 9. Transient pressure distributions on the leeward surface: (*a*) within rotations, and (*b*) post rotations. The switch of the leeward surface in (*b*) is indicated by red boxes.

3.3. *Coexistence of dual mechanisms*

In § 3.2, the coexistence of an attached LEV (within the mid-span) and a BDV system (near the tip) has been evidenced. The downward convection of the attached LEV underneath the upwind surface (figures 6 and 7) occurs in both symmetric and fully advanced rotations, suggesting the existence of the single-vortex suction mechanism. However, the impacts of BDV on local pressure and the underlying mechanism are unclear. To further explain this span dependency of wing–wake interaction, the pressure distributions on the leeward surfaces of both symmetric and fully advanced rotations are compared in figure 9. Note that a switch of the leeward surface occurs when the wing enters the backward stroke (indicated by red boxes). Before the rotations (figure 9*a*), the stable LEV_f can induce a suction region beneath its conical structure. This suction region experiences a continuous attenuation in the symmetric rotation, while that in the advanced rotation first becomes stronger before $\alpha = 90°$, and then shrinks as the rotation proceeds. This transient enhancement of the suction region coincides with the sustained LEV_f growth (figures 6*a*,*c*). As the sweeping decelerates ($\alpha > 90°$), the stronger LEV_f in the advanced rotation can still induce a slight suction region near the leading edge, which is explained by Lua *et al.* (2011) as the single-vortex suction mechanism. In contrast, this phenomenon is trivial in the symmetric pattern due to a remarkably weaker LEV_f.

Another phenomenon observed in both rotations is the local high pressure around the wingtip (figure 9*a*), which is mostly attributed to the BDV impingement towards the upwind surface. Both the stroke deceleration and the nose-down rotation can promote this impingement, thus it becomes more prominent for the symmetric rotation due to the overlapping of these two kinetic features. Unlike the interaction with a single vortex (i.e. the stable LEV_f) explained above, the BDV manifests as a complex vortex system with strong unsteadiness. Although it is laborious to spot detailed elements of this unsteady vortex system, its overall impact is akin to a 'jet' towards the wing, thus resembling the inter-vortex jet mechanism. The difference is that the mechanism proposed by Dickinson (1994) was to explain the interaction with a counter-rotating vortex pair, which can induce an inter-vortex jet towards the surface, thus enlarging the incoming velocity and stagnant pressure. The BDV is certainly different from the counter-rotating vortex pair, but the significant breakdown can slow down the swirling of the vortex system and attenuate
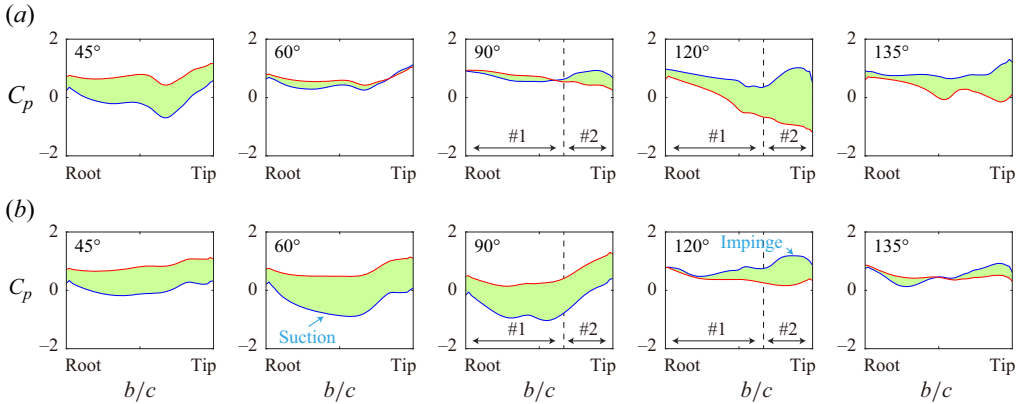
987 A16-14

Figure 10. Sectional pressure force during the rotation: (*a*) symmetric, $\Delta\tau_\alpha = 0.2$, and (*b*) fully advanced, $\Delta\tau_\alpha = 0.2$. The blue and red lines represent the leeward and upwind surfaces in the forward stroke, respectively, and the green mask indicates the net force. Here, #1 and #2 refer to the single-vortex suction and breakdown-vortex jet mechanisms, respectively.

the low pressure in the vortex core. Thus, compared to the impingement of a stable LEV_f (the low pressure inside the vortex is retained), the BDV impingement leads to an exactly opposite pressure variation. This phenomenon is named the breakdown-vortex jet mechanism in this work. Therefore, it is suggested that the wing–wake interaction of a flapping wing at $Re > 10^3$ can be explained mostly by the single-vortex suction and breakdown-vortex jet mechanisms. These two mechanisms may exist simultaneously (but at different spanwise locations) during the wing rotation, especially for an advanced one.

The difference in BDV impingement between the symmetric and advanced rotations also alters the wingtip suction region in the backward stroke (figure 9*b*). For the fully advanced rotation, the wing encounters the BDV at $\alpha = 45°$ without a rotational speed, and the LEV_b near the tip can mostly retain its attachment in the backward stroke (figure 5). Therefore, the suction region near the wingtip is prominent after the advanced rotation at $\lambda = 4.5$, and it is then connected with the suction region induced by the inboard LEV_b. However, due to the stronger BDV impingement in the symmetric rotation (a higher α and a superposition of nose-down rotation), the LEV_b formed by the BDV impingement quickly sheds into the wake during $\lambda = 4.5$–5, and the inboard suction region is then established until $\lambda = 5$–5.5. These explanations relate the superb aerodynamic force during the acceleration of the backward stroke in the advanced rotation (shown in figure 3*b*) to the stronger wingtip suction led by the locally attached LEV (which will be discussed in § 3.4).

The coexistence of single-vortex suction and breakdown-vortex jet mechanisms above the dorsal surface of the wing is further evidenced by the sectional pressure force (figure 10). For the symmetric rotation (figure 10*a*), the low-pressure region induced by the conical LEV on the dorsal surface becomes stronger towards the tip ($\alpha = 45°$, figure 10*a*). As the rotation starts, the LEV intensity and induced low pressure are both attenuated ($\alpha = 60°$–90°, figure 10*a*), but a local pressure reduction still exists within the 0.67 span (#1 region), inferring the suction led by the remaining LEV. However, the dorsal pressure within the 0.33 span from the wing tip (#2 region) is remarkably enhanced, corresponding to the jet of BDV impingement. At $\alpha = 90°$–135°, most lift production originates from the jet mechanism in the #2 region, whereas the suction mechanism in the #1 region dictates the lift generation in the first half of the rotation. Therefore, the single-vortex suction and

987 A16-15

breakdown-vortex jet mechanisms can coexist on a flapping wing during the rotation, but they are located within the stable and unsteady LEV regions, respectively.

The fully advanced rotation case also experiences the coexistence of dual mechanisms during rotation (figure 10b). As less LEV attenuation occurs in the first half of the rotation ($\alpha = 45°$–$90°$), the low-pressure region caused by the suction mechanism (#1 region) is further enhanced. In contrast, the stable high pressure led by the jet of BDV impingement (#2 region, $\alpha = 135°$) is close to that of the symmetric rotation. The only difference related to this high pressure is that the impingement is postponed in the fully advanced rotation. Moreover, despite the fact that the rotation pattern may affect the intensity and phase (with respect to the rotation) of the two mechanisms, their valid ranges along the span are barely changed. This is because these mechanisms are dependent on the LEV status, which is dominated by the local revolving radius (Chen *et al.* 2023b).

3.4. *Lift peak due to breakdown-vortex impingement*

In this subsection, we further focus on the transient lift peak in the acceleration of the backward stroke after fully advanced rotations (see the white circle in figure 3(c), $\tau_{\alpha_0} = 0.5$), and compare it to its counterpart in the forward stroke (without wing–wake interaction). Since this lift peak occurs under an appropriate rotation duration ($\Delta \tau_\alpha > 0.2$), the impact of $\Delta \tau_\alpha$ is also considered here, taking $\Delta \tau_\alpha = 0.1$ and 0.3 as examples. The transient 3-D vortex structures and pressure distributions during $\lambda = 4$–4.5 (backward stroke) and $\lambda = 0$–0.5 (forward stroke) are compared in figure 11. During $\lambda = 0$–0.5 (figure 11a), the typical vortex structures are in a perfect ring shape along the edges, and the conical LEV$_f$ almost covers the entire span. However, in the backward stroke, regardless of $\Delta \tau_\alpha$ (figures 11b,c), the LEV$_b$ cannot achieve a comparable conical structure along the span but mostly concentrates near the wingtip at $\lambda = 4.25$. This is attributed to the BDV impingement, the majority of which is located near the distal end of the wing. Comparing the BDV structures at the beginning of the backward stroke ($\lambda = 4$ in figures 11b,c), they are stronger and more coherent at $\Delta \tau_\alpha = 0.3$. This implies that a milder advanced rotation ($\Delta \tau_\alpha = 0.3$) can alleviate the dissipation and breakdown of this complex vortex structure. These stronger wake vortices further induce an intensified interaction with the wing, leading to a stronger LEV$_b$ and TV$_b$ system ($\lambda = 4.25$).

As shown by the transient pressure at $\lambda = 0.25$ (figure 11d), corresponding to the lift peak without BDV impingement, an LEV$_f$-induced suction region is observed along the leading edge. Together with the gradual increment of high pressure (on the upwind surface) along the span, the lift peak at $\lambda = 0.25$ originates mostly from the leading-edge region. In contrast, due to the BDV impingement in the backward stroke, the high-lift region is further confined near the wingtip, and extends along the chord. The reasons for these variations are twofold. First, due to the LEV$_b$ concentration near the wingtip, the suction force on the leeward surface is confined near the intersection of the leading edge and wingtip. Second, due to the impingement of BDV in the wake, the high pressure on the upwind surface experiences a more prominent increase in the outboard region of the wing. As the advanced rotation becomes milder and thus the LEV$_b$ and BDV are stronger, these two phenomena are more remarkable. Therefore, the transient lift peak due to BDV impingement in a fully advanced rotation (during the acceleration of the backward stroke) becomes intensified as $\Delta \tau_\alpha$ increases to 0.3 (figure 3c).

A closer examination of the wing-tip vortex structures and the flow patterns with/without BDV impingement is shown in figure 12. Comparing figures 12(a) and 12(b), regardless of $\Delta \tau_\alpha$, the BDV impingement can intensify the local radial vorticity
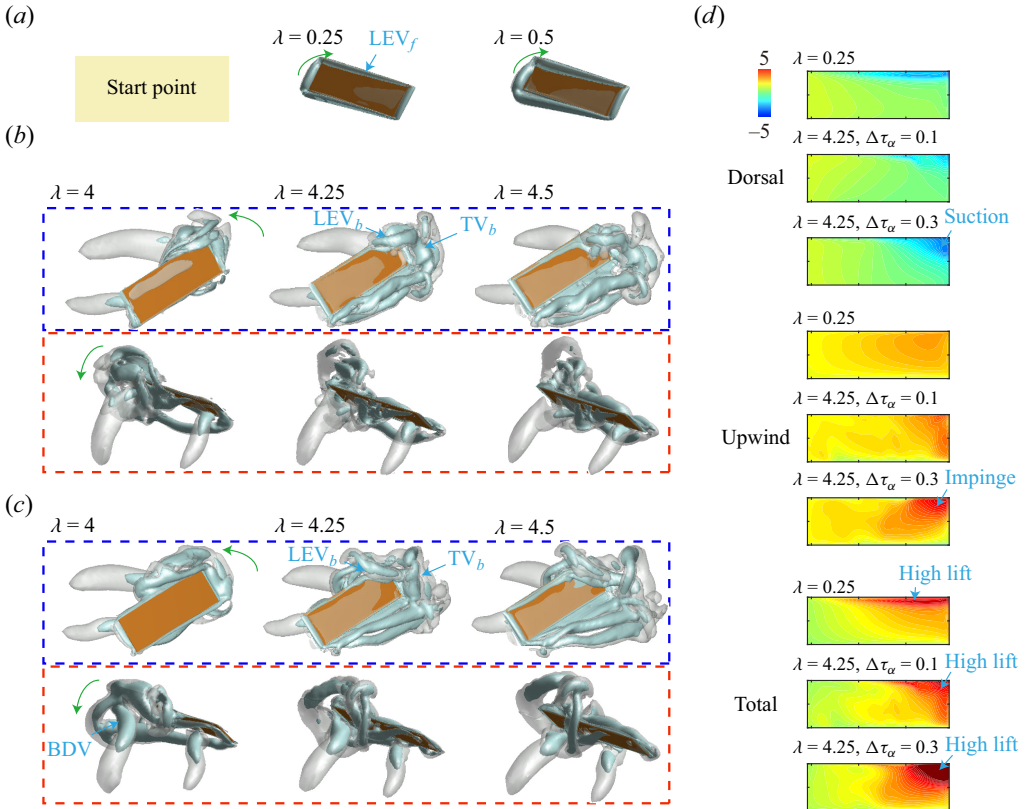
Figure 11. Vortex structure and pressure distribution with/without wing–wake interaction in a fully advanced rotation: (*a*) vortex structure without interaction, (*b*) vortex structure with interaction at $\Delta\tau_\alpha = 0.1$, (*c*) vortex structure with interaction at $\Delta\tau_\alpha = 0.3$, and (*d*) pressure distributions. The blue and red boxes represent different camera views, and the green arrow denotes the sweep direction.
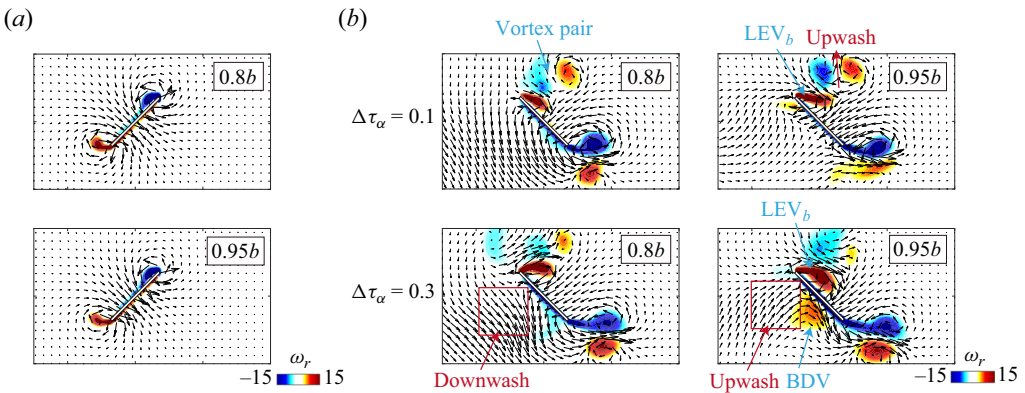

Figure 12. Radial vorticity and flow vectors near the wingtip during an advanced rotation: (*a*) $\lambda = 0.25$ (without breakdown-vortex impingement), and (*b*) $\lambda = 4.25$ (with breakdown-vortex impingement).

inside the LEV between $0.8b$ and $0.95b$. Moreover, the LEV_b at $\Delta\tau_\alpha = 0.3$ is slightly stronger between $0.8b$ and $0.95b$, and further approaches the leeward surface. In contrast, the LEV_b at $\Delta\tau_\alpha = 0.1$ is lifted from the surface at $0.95b$, which can be explained by additional upwash induced by the wake vortex pair above the LEV_b (see the $0.95b$ slice

987 A16-17

in figure 12*b*). Usually, a strong downwash is established in the wake of flapping wings (e.g. 0.8*b* slice in figure 12*b*). The local upwash can mediate the existing downwash, and thus leads to a further tangential elongation of the LEV$_b$, and induces a lower suction force on the leeward surface (figure 11*d*). A similar but weaker upwash is also observed on the 0.8*b* slice at $\Delta\tau_\alpha = 0.3$ due to the pass-by of a vortex pair. In addition, there is another obvious interaction between the upwind surface and the residual BDV. According to the flow field outlined by red boxes in figure 12(*b*), the approaching of this residual BDV reverses the downwash ahead of the wing to a comparable upwash, which triggers the breakdown-vortex jet that causes the local high-pressure region on the upwind surface.

3.5. *Extension to previous works and limitation*

Previous 3-D studies on the wing–wake interaction mostly focus on fruitfly wings at *Re* close to 100 (Sun & Tang 2002; Birch & Dickinson 2003; Wu & Sun 2005; Kweon & Choi 2010; Lee & Lua 2018). Compared to the present work, almost no LEV breakdown occurs in the outboard region at $Re \sim 10^2$. This unsteady LEV feature at $Re > 10^3$ may introduce a locally novel wing–wake interaction phenomenon during the wing rotation, which is one of the motivations of this work. Our force analysis found that an advanced rotation enhances the overall lift of a flapping wing with these unsteady LEV features at *Re* up to over 10^3. Similarly, delayed rotations are still detrimental to lift generation at $Re > 10^3$.

Upon the inter-vortex jet mechanism (Dickinson 1994), despite the unsteady mix-up of LEV and TV in the outboard region, there is no strong evidence for the pair-up of LEV and TEV. Thus this mechanism may not be appropriate to explain the remarkably high pressure on the upwind surface. However, the residual breakdown vortex in the outboard region is strong and can also impinge towards the upwind surface, resulting in a phenomenon similar to the inter-vortex jet (figure 12*b*). In general, the impingement of the breakdown vortex always leads to a local high pressure for both symmetric and advanced rotations (figure 9*a*). This mechanism is novel for flapping wings at *Re* up to over 10^3 and is thus named as the breakdown-vortex jet mechanism. In contrast, the interaction between the stable LEV in the inboard region and the wing leads to a reduced pressure (figure 9*a*), equivalent to the single-vortex suction mechanism proposed by Lua *et al.* (2011). These findings support that the wing–wake interaction during the rapid rotation of 3-D flapping wings at $Re > 10^3$ is dependent on the local LEV state. More importantly, the breakdown-vortex jet (beneficial) and single-vortex suction (detrimental) mechanisms may occur simultaneously but within different spanwise regions.

In the 3-D simulations done by Lee & Lua (2018), the wing–wake interaction at $Re = 10^2$ is explained by four mechanisms, among which the LEV shedding due to vortex pairing (detrimental) and the formation of a closely attached LEV (beneficial) are unique for a 3-D flapping wing. In our research, the first mechanism is absent in both symmetric and advanced rotations since the stable LEV generated in the inboard region of the wing is convected towards the trailing edge and then merges with the newly formed TEV (figures 6*b*,*d*), instead of pairing up with the new LEV near the leading edge. The second mechanism implies that the wake can improve the LEV attachment by inducing a downwash, and thus increases the lift generation after the mid-stroke. Apart from the explanation proposed by Lee & Lua (2018), the downwash effect around the mid-stroke is mostly regarded to be adverse to lift generation (Sun & Tang 2002; Oh *et al.* 2020; Cai *et al.* 2021). This is because the downwash can reduce the effective angle of attack of the wing. Although the interactive effects of wings and downwash around the mid-stroke

987 A16-18

are not the focus of this work, our data show that the lift profiles after the mid-stroke of both forward and backward strokes are almost identical for symmetric rotations (figure 3c). This observation is retained in the following ten flapping cycles (lift profiles over multiple flapping cycles are provided in the Appendix). Together with the contradictory findings of Lee & Lua (2018), Sun & Tang (2002), Oh *et al.* (2020) and Cai *et al.* (2021), our results indicate that the specific contribution of the wing–downwash interaction to lift generation may be sensitive to wing kinematics.

Although a slight lift enhancement occurs over the same period after an advanced rotation, it is suggested that due to the distinct LEV states in the inboard and outboard regions, the local wing–wake interaction may involve a remarkable spatial difference in the specific mechanism. Evidence for this is the upwash, rather than a downwash, existing above the wing-tip LEV after an advanced rotation (figure 12b). This upwash is induced by a vortex pair originating from the breakdown vortex generated in the previous stroke. Due to the strong unsteadiness of this vortex structure and its dependency on wing kinematics, the location of this upwash along the span is closely associated with $\Delta\tau_\alpha$. Again, once this upwash replaces the downwash, the fourth mechanism proposed in Lee & Lua (2018) is locally invalid since the LEV_b is lifted from the surface and the suction force is thus reduced.

As suggested by Wu & Sun (2005) and Lee & Lua (2018), the contribution of wing–wake interaction on the lift generation of 3-D flapping wings is strongly related to wing kinematics and may even be a case-by-case problem. Within this research, the effects of rotation duration and phase relative to the stroke are examined, while no discussion on sweep kinematics is involved. Future studies can conduct a coupled variation of sweep and rotation kinematics, and further justify our findings in a broader parameter space. Moreover, our previous works on the LEV dynamics of flapping wings have quantified the connection between local LEV status with wing kinematics covering a wide space over *Re*, *AR*, and *Ro* (Chen *et al.* 2022a, 2023b). An extension for the quantitative connection between local LEV status and the mechanisms of wing–wake interaction is encouraged. Due to the strong unsteadiness in the wing–wake interaction, an explicit model can be impractical, and black-box models using machine learning, e.g. deep neural networks, should be more efficient.

4. Conclusion

The aerodynamic lift and underlying vorticity dynamics during the rapid wing rotation of a low aspect ratio flapping wing at $Re = 1500$ are investigated using numerical simulations, focusing on novel wing–wake interaction phenomena led by distinct leading-edge vortex (LEV) states (attached or breakdown) between the inboard and outboard regions. The wing is simplified as a rectangular plate, and undergoes a reciprocating sweeping motion with a trapezoidal profile. To focus on the discrepancies caused by the wing–wake interaction, the forward and backward strokes in the first cycle are considered. The wing rotates around the mid-chord near the stroke reversal, following a similar trapezoidal profile. To ensure a fully developed LEV, the stroke amplitude is 4 chord lengths of travel at the radius of gyration, and the constant angle of attack in both half-strokes is $45°$. Our results show that despite LEV breakdown and mix-up with tip vortex in the outboard region, an advanced rotation still enhances the averaged lift generation of the flapping wing, which is more prominent for a steeper rotation. In contrast, an obvious lift loss occurs when the wing takes a delayed rotation. The wing–wake interaction during a wing rotation at $Re \sim 10^3$ can be explained mainly by two mechanisms, i.e. the single-vortex
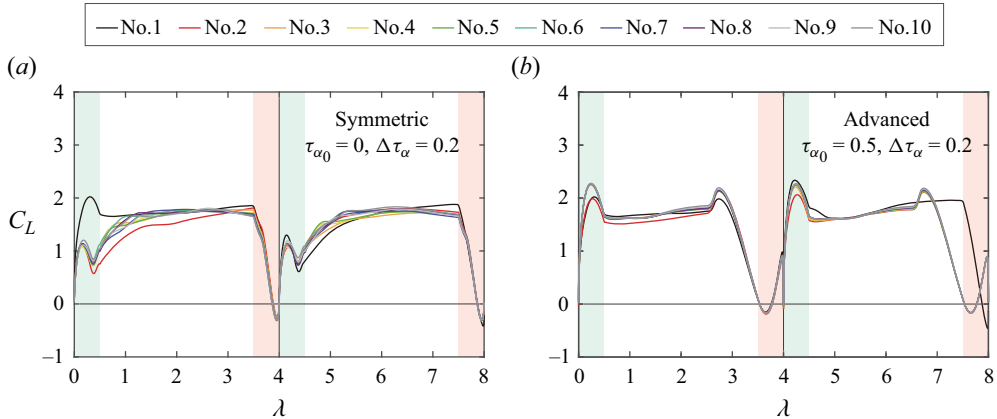
Figure 13. Transient lift in the first ten cycles of flapping wings. The data for the first cycle are duplicated from data in figure 3.

suction mechanism and a novel breakdown-vortex jet mechanism, that work in the inboard and outboard regions, respectively. The first mechanism is attributed to the convection of the stable LEV underneath the upwind surface, which is mostly detrimental to lift enhancement in both symmetric and advanced rotations. The second mechanism features the breakdown-vortex impingement and thus a local jet towards the upwind surface. This jet is akin to the inter-vortex jet, but no evidence for a vortex pair is observed. Moreover, the impinging timing with respect to the sweeping can affect the LEV dynamics in the following half-stroke. Due to the accomplishment of nose-down rotation, a flapping wing with fully advanced rotation can take advantage of an attached LEV near the wingtip and a higher stagnation pressure on the upwind surface, leading to an obvious lift peak in the early stage of the backward stroke. The vortical structures under symmetric and advanced rotations are then explained via an analysis of vorticity transport. These findings on flow patterns prove that the single-vortex suction and breakdown-vortex jet mechanisms can occur simultaneously in the stable/breakdown LEV of a flapping wing. Compared to cases at $Re \sim 10^2$, the wing geometry and kinematics that determine the unsteady LEV features at $Re = 1500$ may be more critical to assess the wing–wake interaction.

Declaration of interests. The authors report no conflict of interest.

Data availability statement. The data are available from the corresponding author upon reasonable request.

Author ORCIDs.
Ⓑ Long Chen https://orcid.org/0000-0002-0222-2665;
Ⓑ Jianghao Wu https://orcid.org/0000-0002-1642-0910.

Author contributions. L.C.: conceptualization (equal); funding acquisition (equal); investigation; methodology; validation; writing – original draft. J.W.: conceptualization (equal); funding acquisition (equal); project administration; resources; supervision; writing – review and editing.

Appendix

The transient lifts in the first ten cycles of flapping wings with symmetric rotation ($\tau_{\alpha_0} = 0$) and fully advanced rotation ($\tau_{\alpha_0} = 0.5$) are shown in figure 13. In both cases, the

variation of transient lift reaches a periodic state at the third flapping cycle. Note that an obvious deviation occurs in the fully advanced case when λ is 7–8. This is because, in our analysis based on one flapping cycle, no rotation is designed at the end of the backward stroke.

REFERENCES

AONO, H., LIANG, F. & LIU, H. 2008 Near- and far-field aerodynamics in insect hovering flight: an integrated computational study. *J. Expl Biol.* **211** (2), 239–257.

BIRCH, J.M. & DICKINSON, M.H. 2001 Spanwise flow and the attachment of the leading-edge vortex on insect wings. *Nature* **412** (6848), 729–733.

BIRCH, J.M. & DICKINSON, M.H. 2003 The influence of wing–wake interactions on the production of aerodynamic forces in flapping flight. *J. Expl Biol.* **206** (13), 2257–2272.

CAI, X., KOLOMENSKIY, D., NAKATA, T. & LIU, H. 2021 A CFD data-driven aerodynamic model for fast and precise prediction of flapping aerodynamics in various flight velocities. *J. Fluid Mech.* **915**, A114.

CHEN, L., WANG, L., ZHOU, C., WU, J. & CHENG, B. 2022*a* Effects of Reynolds number on leading-edge vortex formation dynamics and stability in revolving wings. *J. Fluid Mech.* **931**, A13.

CHEN, L., WU, J. & CHENG, B. 2019 Volumetric measurement and vorticity dynamics of leading-edge vortex formation on a revolving wing. *Exp. Fluids* **60**, 1–15.

CHEN, L., WU, J. & CHENG, B. 2020 Leading-edge vortex formation and transient lift generation on a revolving wing at low Reynolds number. *Aerosp. Sci. Technol.* **97**, 105589.

CHEN, L., WU, J., ZHOU, C., HSU, S.-J. & CHENG, B. 2018 Unsteady aerodynamics of a pitching-flapping-perturbed revolving wing at low Reynolds number. *Phys. Fluids* **30** (5), 051903.

CHEN, L., ZHANG, Y., ZHOU, C. & WU, J. 2023*a* Vorticity dynamics of fully developed leading-edge vortices on revolving wings undergoing pitch-up maneuvers. *Phys. Fluids* **35** (3), 031904.

CHEN, L., ZHOU, C., WERNER, N.H., CHENG, B. & WU, J. 2023*b* Dual-stage radial–tangential vortex tilting reverses radial vorticity and contributes to leading-edge vortex stability on revolving wings. *J. Fluid Mech.* **963**, A29.

CHEN, Z., LI, X. & CHEN, L. 2022*b* Enhanced performance of tandem plunging airfoils with an asymmetric pitching motion. *Phys. Fluids* **34** (1), 011910.

CHENG, B., SANE, S.P., BARBERA, G., TROOLIN, D.R., STRAND, T. & DENG, X. 2013 Three-dimensional flow visualization and vorticity dynamics in revolving wings. *Exp. Fluids* **54**, 1–12.

CHENG, X. & SUN, M. 2019 Revisiting the clap-and-fling mechanism in small wasp *Encarsia formosa* using quantitative measurements of the wing motion. *Phys. Fluids* **31** (10), 101903.

CHIN, D.D. & LENTINK, D. 2016 Flapping wing aerodynamics: from insects to vertebrates. *J. Expl Biol.* **219** (7), 920–932.

DASH, S.M., LUA, K.B., LIM, T.T. & YEO, K.S. 2018 Enhanced thrust performance of a two dimensional elliptic airfoil at high flapping frequency in a forward flight. *J. Fluids Struct.* **76**, 37–59.

DICKINSON, M.H. 1994 The effects of wing rotation on unsteady aerodynamic performance at low Reynolds numbers. *J. Expl Biol.* **192** (1), 179–206.

DICKINSON, M.H., LEHMANN, F.-O. & SANE, S.P. 1999 Wing rotation and the aerodynamic basis of insect flight. *Science* **284** (5422), 1954–1960.

ELLINGTON, C.P. 1984 The aerodynamics of hovering insect flight. III. Kinematics. *Phil. Trans. R. Soc. Lond.* B **305** (1122), 41–78.

ELLINGTON, C.P., VAN DEN BERG, C., WILLMOTT, A.P. & THOMAS, A.L.R. 1996 Leading-edge vortices in insect flight. *Nature* **384** (6610), 626–630.

GARMANN, D.J., VISBAL, M.R. & ORKWIS, P.D. 2013 Three-dimensional flow structure and aerodynamic loading on a revolving wing. *Phys. Fluids* **25** (3), 034101.

JARDIN, T. 2017 Coriolis effect and the attachment of the leading edge vortex. *J. Fluid Mech.* **820**, 312–340.

JARDIN, T. & DAVID, L. 2014 Spanwise gradients in flow speed help stabilize leading-edge vortices on revolving wings. *Phys. Rev.* E **90** (1), 013011.

JEONG, J. & HUSSAIN, F. 1995 On the identification of a vortex. *J. Fluid Mech.* **285**, 69–94.

KIM, D. & CHOI, H. 2007 Two-dimensional mechanism of hovering flight by single flapping wing. *J. Mech. Sci. Technol.* **21**, 207–221.

KWEON, J. & CHOI, H. 2010 Sectional lift coefficient of a flapping wing in hovering motion. *Phys. Fluids* **22** (7), 071703.

LEE, Y.J. & LUA, K.B. 2018 Wing–wake interaction: comparison of 2D and 3D flapping wings in hover flight. *Bioinspir. Biomim.* **13** (6), 066003.

LEHMANN, F.-O. 2008 When wings touch wakes: understanding locomotor force control by wake–wing interference in insect wings. *J. Expl Biol.* **211** (2), 224–233.

LENTINK, D. & DICKINSON, M.H. 2009 Rotational accelerations stabilize leading edge vortices on revolving fly wings. *J. Expl Biol.* **212** (16), 2705–2719.

LI, H. & NABAWY, M.R.A. 2022 Capturing wake capture: a 2D numerical investigation into wing–wake interaction aerodynamics. *Bioinspir. Biomim.* **17** (6), 066015.

LIM, T.T., TEO, C.J., LUA, K.B. & YEO, K.S. 2009 On the prolong attachment of leading edge vortex on a flapping wing. *Mod. Phys. Lett.* B **23** (3), 357–360.

LUA, K.B., LEE, Y.J., LIM, T.T. & YEO, K.S. 2016*a* Aerodynamic effects of elevating motion on hovering rigid hawkmothlike wings. *AIAA J.* **54** (8), 2247–2264.

LUA, K.B., LEE, Y.J., LIM, T.T. & YEO, K.S. 2017 Wing–wake interaction of three-dimensional flapping wings. *AIAA J.* **55** (3), 729–739.

LUA, K.B., LIM, T.T. & YEO, K.S. 2011 Effect of wing–wake interaction on aerodynamic force generation on a 2D flapping wing. *Exp. Fluids* **51**, 177–195.

LUA, K.B., LU, H., ZHANG, X.H., LIM, T.T. & YEO, K.S. 2016*b* Aerodynamics of two-dimensional flapping wings in tandem configuration. *Phys. Fluids* **28** (12), 121901.

LUA, K.B., ZHANG, X.H., LIM, T.T. & YEO, K.S. 2015 Effects of pitching phase angle and amplitude on a two-dimensional flapping wing in hovering mode. *Exp. Fluids* **56**, 1–22.

OH, S., LEE, B., PARK, H., CHOI, H. & KIM, S.-T. 2020 A numerical and theoretical study of the aerodynamic performance of a hovering rhinoceros beetle (*trypoxylus dichotomus*). *J. Fluid Mech.* **885**, A18.

POELMA, C., DICKSON, W.B. & DICKINSON, M.H. 2006 Time-resolved reconstruction of the full velocity field around a dynamically-scaled flapping wing. *Exp. Fluids* **41**, 213–225.

SHYY, W. & LIU, H. 2007 Flapping wings and aerodynamic lift: the role of leading-edge vortices. *AIAA J.* **45** (12), 2817–2819.

SINHA, J., LUA, K.B. & DASH, S.M. 2021 Influence of the pivot location on the thrust and propulsive efficiency performance of a two-dimensional flapping elliptic airfoil in a forward flight. *Phys. Fluids* **33** (8), 081912.

SUN, M. & LAN, S.L. 2004 A computational study of the aerodynamic forces and power requirements of dragonfly (*aeschna juncea*) hovering. *J. Expl Biol.* **207** (11), 1887–1901.

SUN, M. & TANG, J. 2002 Unsteady aerodynamic force generation by a model fruit fly wing in flapping motion. *J. Expl Biol.* **205** (1), 55–70.

SUN, M. & WU, J. 2004 Large aerodynamic forces on a sweeping wing at low Reynolds number. *Acta Mechanica Sin.* **20** (1), 24–31.

WEIS-FOGH, T. 1973 Quick estimates of flight fitness in hovering animals, including novel mechanisms for lift production. *J. Expl Biol.* **59** (1), 169–230.

WERNER, N.H., CHUNG, H., WANG, J., LIU, G., CIMBALA, J.M., DONG, H. & CHENG, B. 2019 Radial planetary vorticity tilting in the leading-edge vortex of revolving wings. *Phys. Fluids* **31** (4), 041902.

WU, J., CHEN, L., ZHOU, C., HSU, S.-J. & CHENG, B. 2019 Aerodynamics of a flapping-perturbed revolving wing. *AIAA J.* **57** (9), 3728–3743.

WU, J. & SUN, M. 2005 The influence of the wake of a flapping wing on the production of aerodynamic forces. *Acta Mechanica Sin.* **21** (5), 411–418.

WU, J.-Z., MA, H.-Y. & ZHOU, M.-D. 2007 *Vorticity and Vortex Dynamics*. Springer Science & Business Media.